İSTANBUL UNIVERSITY CERRAHPAŞA

ORIGINAL ARTICLE
Electrica 2025; 25: 1-10

Beam-Squint-Aware Statistical Reconfigurable Intelligent Surface Beamforming Under Amplitude–Phase–Frequency Coupling for Dual Wideband Channels

Hakan Özen, Gökhan Güvensen

Department of Electrical & Electronics Engineering, Middle East Technical University Faculty of Engineering, Ankara, Türkiye

Cite this article as: H. Özen and G. M. Güvensen, "Beam-squint-aware statistical RIS beamforming under amplitude–phase–frequency coupling for dual wideband channels," *Electrica*, 25, 0154, 2025. doi: 10.5152/electrica.2025.24154.

WHAT IS ALREADY KNOWN ON THIS TOPIC?

- *The literature indicates that the reflection characteristics of practical reconfigurable intelligent surfaces (RISs) follow a model in which the amplitude and phase of the reflection coefficient are coupled. This coupling also depends on the frequency of the incoming electromagnetic wave, a phenomenon referred to as amplitude-phase-frequency-coupling (APFC).*
- *However, most existing RIS beamforming studies assume an ideal reflection model and overlook the APFC inherent in practical RIS elements.*

Corresponding: Gökhan M. Güvensen

E-mail:
guvensen@metu.edu.tr

Received: November 8, 2024
Revision Requested: January 5, 2025
Last Revision Received: January 27, 2025
Accepted: February 4, 2025
Publication Date: April 28, 2025

DOI: 10.5152/electrica.2025.24154

ABSTRACT

In this paper, the amplitude–phase–frequency coupling (APFC) constraint in practical reconfigurable intelligent surfaces (RISs) is first investigated. Building on this, three distinct beam-squint-aware and APFC-aware statistical quantized RIS designs are proposed for frequency- and spatial-wideband (dual-wideband) RIS-aided massive multiple-input multiple-output systems, optimized respectively for signal-to-noise ratio, mean statistical mutual information, and the ergodic capacity upper bound based on the cascaded channel covariance matrix. To optimize these metrics, an iterative alternating optimization (AO) algorithm, referred to as the iterative phase refinement algorithm, is adopted, which converges in just a few iterations. Simulation results show that the proposed RIS beamforming designs outperform conventional approaches in terms of spectral efficiency and outage capacity.

Index Terms—Amplitude–phase–frequency coupling, beam-squint, reconfigurable intelligent surfaces, statistical beamforming

I. INTRODUCTION

Reconfigurable intelligent surfaces (RISs) have emerged as a transformative technology in wireless communication [1, 2]. Composed of passive reflecting elements, these surfaces can manipulate the propagation of electromagnetic waves. By dynamically adjusting the phase of each element, RISs can create controllable wireless environments. This innovative approach shows great potential for future wireless networks, offering improvements in spectral efficiency (SE), energy efficiency, and enabling a broad array of applications [3].

In literature, many studies assume ideal reflection responses for RIS structures [4–7]. This assumption entails that each RIS element possesses unit amplitude, and that the phase of any RIS element can be freely adjusted. However, practical implementation reveals that this assumption is not applicable due to the inherent coupling between the amplitude and phase of individual RIS elements [8]. Furthermore, this interrelationship extends to the frequency of the incoming electromagnetic wave, a phenomenon referred to as amplitude–phase–frequency coupling (APFC) [9, 10].

Many studies have explored continuous phase designs for RIS elements, but these approaches present practical challenges due to the need for sophisticated and costly hardware [11]. Continuous phase adjustment requires a complex infrastructure, with multiple control pins connected to each element [12]. This complexity undermines the fundamental goal of RISs, which is to offer a low-cost, easily deployable solution. To address these practical issues, discrete phase shift designs are often preferred [13]. In this approach, each RIS element is connected to a small number of positive-intrinsic-negative (PIN) diodes, and the required phase shifts are achieved by controlling the on/off states of these diodes through control signals [14].

Reconfigurable intelligent surface deployments often consist of a large number of elements, as noted in ref. [15], making computational overhead a critical concern for practical systems. Many

WHAT DOES THIS STUDY ADD ON THIS TOPIC?

- *To the best of the authors' knowledge, this study is the first to propose statistical RIS beamforming designs that explicitly account for both the amplitude-phase-frequency coupling (APFC) and the beam-squint effect in dual-wideband RIS-aided massive MIMO systems.*
- *Simulation results show that neglecting the APFC can result in up to 5 dB power loss to achieve the same spectral efficiency.*

studies propose RIS optimization algorithms based on instantaneous channel state information (I-CSI) [16-18]. However, due to the fast-varying nature of channel gains, I-CSI can change rapidly, leading to frequent configuration updates and significant computational overhead in I-CSI-based designs. In contrast, statistical RIS designs exploit slowly-varying channel parameters, such as path angles, and do not rely on I-CSI. Path angles evolve at a much slower rate than path gains, as noted in ref. [19–21]. A new concept, angular coherence time, has been introduced to describe the extended period during which path angles remain nearly constant [22]. Measurements show that angular coherence time can be significantly longer than traditional channel coherence time [22]. Consequently, statistical RIS designs, which only require updates at each angular coherence time, eliminate the need for frequent adjustments and significantly reduce computational overhead.

Studies have demonstrated that a large RIS comprising N reflecting elements can boost the signal-to-noise ratio (SNR) by a factor of $O(N^2)$, a phenomenon referred to as the "square law", thereby substantially enhancing signal quality at the receiver [12]. However, as the number of RIS elements increases, the propagation delay across the RIS array becomes comparable to the symbol duration [23, 24]. This leads to the beam-squint effect (BSE), where different subcarriers experience distinct angles of arrival (AoAs) and angles of departure (AoDs) for the same physical path [23, 24]. If not properly addressed, the BSE can lead to significant performance degradation [25].[1]

The literature review reveals that many RIS beamforming studies assume ideal RIS responses, adopt continuous phase designs, and rely on I-CSI-based designs. Additionally, the APFC constraint and the BSE have received limited attention. To address these gaps, statistical quantized RIS designs are proposed that account for both the BSE and the APFC for dual-wideband RIS-aided massive multiple-input multiple-output (MIMO) systems. The key contributions are as follows:

- The APFC constraint inherent in RIS structures is investigated, demonstrating how the amplitude and phase of RIS elements change in response to the frequency of incoming signals.
- Quantized RIS designs are proposed, and simulation results indicate that the 4-bit quantized RIS closely matches the SE of its unquantized counterpart for dual-wideband channels under the APFC constraint.
- Signal-to-noise ratio-based, statistical mutual information (SMI)-based, and cascaded channel covariance matrix (C-CCM)-based statistical RIS designs are introduced that do not rely on I-CSI. These designs account for both the BSE and the APFC. To the best of the authors' knowledge, this is the first study to propose a statistical RIS design considering both BSE and APFC. Simulation results show that the proposed designs outperform conventional approaches that overlook these effects in terms of SE and outage capacity.

Notations: Fonts x, $\mathbf{x}$, and $\mathbf{X}$ represent scalars, column vectors, and matrices, respectively. The complex conjugate and magnitude of x are denoted by x^* and $|x|$, respectively. The determinant, inverse, transpose, and Hermitian of $\mathbf{X}$ are represented by $\det|\mathbf{X}|$, $\mathbf{X}^{-1}$, $\mathbf{X}^{\mathrm{T}}$, and $\mathbf{X}^{\mathrm{H}}$, respectively. The ith element of $\mathbf{x}$ and the (i, j)th entry of $\mathbf{X}$ are denoted as $[\mathbf{x}]_{(i)}$ and $[\mathbf{X}]_{(i,j)}$, respectively. The ℓ_2-norm is represented by $\mathbf{x}$. The notations $\mathbf{I}_D$ and $0_{D\times 1}$ refer to the $D \times D$ identity matrix and the $D \times 1$ all-zeros vector, respectively. Lastly, $\mathbb{E}\{\cdot\}$, $\mathrm{Tr}\{\cdot\}$, $\lfloor . \rfloor$, and δ_{ij} represent the expectation operator, trace operator, floor function, and Kronecker delta, respectively.

II. AMPLITUDE–PHASE–FREQUENCY COUPLING

Reconfigurable intelligent surface structures are typically fabricated using printed circuit boards that incorporate metallic elements on dielectric substrates [9, 10, 26]. Additionally, these structures often integrate semiconductor devices, such as PIN diodes, to fine-tune reflection responses by manipulating impedance [9, 10, 26]. Achieving accurate modeling of the reflection response

1 Some concepts from this paper were covered in an earlier conference paper [25]. In ref. [25], the focus was on the interference suppression capability of RIS under dual-wideband channels, but the frequency dependence of the amplitude–phase coupling was neglected, which is a primary focus in this paper. Moreover, [25] considered only line-of-sight (LOS) paths between the BS-RIS and RIS-UE (i.e., L = J = 1), while this work adopts a more generic channel model (i.e., L > 1 and J > 1). Additionally, a novel RIS design metric is introduced in this paper, which considers the amplitude–phase–frequency coupling, referred to as the C-CCM-based RIS design.

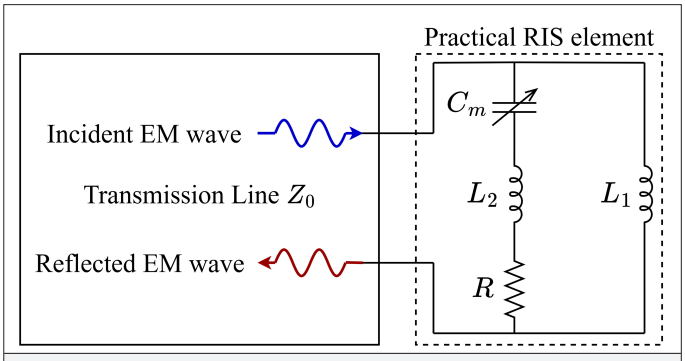

Fig. 1. The equivalent circuit of a practical RIS element.

of an RIS element is accomplished through an equivalent parallel resonant circuit as depicted in Fig. 1 [8]. Let $\phi(f)\in\mathbb{C}^{N\times 1}$ denote the reflection coefficients of an *N*-element RIS for an incident signal with frequency *f*. The impedance of the *m*th element of the practical RIS then can be given as [8]

$$Z(C_m,f)=\frac{i2\pi fL_1\left(i2\pi fL_2+\frac{1}{i2\pi fC_m}+R\right)}{i2\pi fL_1+\left(i2\pi fL_2+\frac{1}{i2\pi fC_m}+R\right)}, \tag{1}$$

where f, L_1, L_2, C_m, and R are the frequency of the incident signal, bottom layer inductance, top layer inductance, effective capacitance and the loss resistance, respectively. The reflection coefficient of the *m*th element then can be expressed as [8]

$$\left[\phi(f)\right]_{(m)}=\frac{Z(C_m,f)-Z_0}{Z(C_m,f)+Z_0}, \tag{2}$$

where Z_0 is the free space impedance. To control the reflection coefficient $[\phi(f)]_{(m)}$, one can vary the effective capacitance C_m to manipulate the reflected electromagnetic waves. As evident from (2), the amplitude and phase of the reflection coefficient $[\phi(f)]_{(m)}$, are intrinsically intertwined, and they cannot be adjusted independently.

Fig. 2 illustrates the APFC effect. First, the amplitude is plotted against the phase for different values of the incident signal frequency. To create this plot, the capacitance C_m is varied from 0.47 pF to 2.35 pF, aligning with the experimental setup in ref. [8]. Other parameters remain constant, including $L_1=2.5$ nH, $L_2=0.7$ nH, $R=2.5$ Ω, and $Z_0=377$ Ω, as specified in ref. [8]. Next, the amplitude and phase are depicted against the incident wave's frequency for varying values of capacitance C_m. These figures demonstrate that the reflection response of the RIS exhibits significant variation with changing frequencies, which could potentially lead to considerable performance degradation when dealing with wideband incident signals if not properly addressed.

III. SYSTEM MODEL

An uplink scenario for dual-wideband channels is considered, where a base station (BS) with an *M*-antenna uniform linear array (ULA) serves a single-antenna user equipment (UE) located in the far field via an *N*-element ULA-type RIS. It is assumed that no direct path exists between the BS and the UE.

The received signal at the BS in the frequency domain for the *k*th subcarrier can be expressed as [27, 28]

$$\mathbf{y}_k=\mathbf{H}_k\mathrm{diag}(\phi_k)\mathbf{h}_k x_k+\mathbf{n}_k\in\mathbb{C}^{M\times 1}, \tag{3}$$

for $k=1,2,\ldots,N_c$ where N_c is the number of subcarriers, $\mathbf{H}_k\in\mathbb{C}^{M\times N}$ represents the frequency domain channel matrix between the BS and RIS, $\phi_k\in\mathbb{C}^{N\times 1}$ represents the frequency-dependent reflection coefficients of the RIS for an incident signal with frequency f_k, $\mathbf{h}_k\in\mathbb{C}^{N\times 1}$ represents the frequency domain channel vector between the RIS and UE, x_k represents the transmitted orthogonal frequency-division multiplexing symbol of the UE, and $\mathbf{n}_k\in\mathbb{C}^{M\times 1}$ is a zero-mean complex random Gaussian noise vector that satisfies $\mathbb{E}\{\mathbf{n}_k\mathbf{n}_{k'}^H\}=N_0\mathbf{I}_M\delta_{kk'}$. The transmitted symbols are assumed to be uncorrelated, i.e., $\mathbb{E}\{x_k x_{k'}^*\}=\delta_{kk'}$.

The spatial wideband BS-RIS and RIS-UE channels can be expressed in the frequency domain as [27, 28]

$$\mathbf{H}_k=\sum_{\ell=1}^{L}\bar{\alpha}_\ell\bar{\mathbf{u}}_k(\theta_\ell)\mathbf{u}_k^H(\varphi_\ell)e^{-i2\pi f_k\bar{\tau}_\ell}\in\mathbb{C}^{M\times N}, \tag{4}$$

$$\mathbf{h}_k=\sum_{j=1}^{J}\alpha_j\mathbf{u}_k(\vartheta_j)e^{-i2\pi f_k\tau_j}\in\mathbb{C}^{N\times 1}, \tag{5}$$

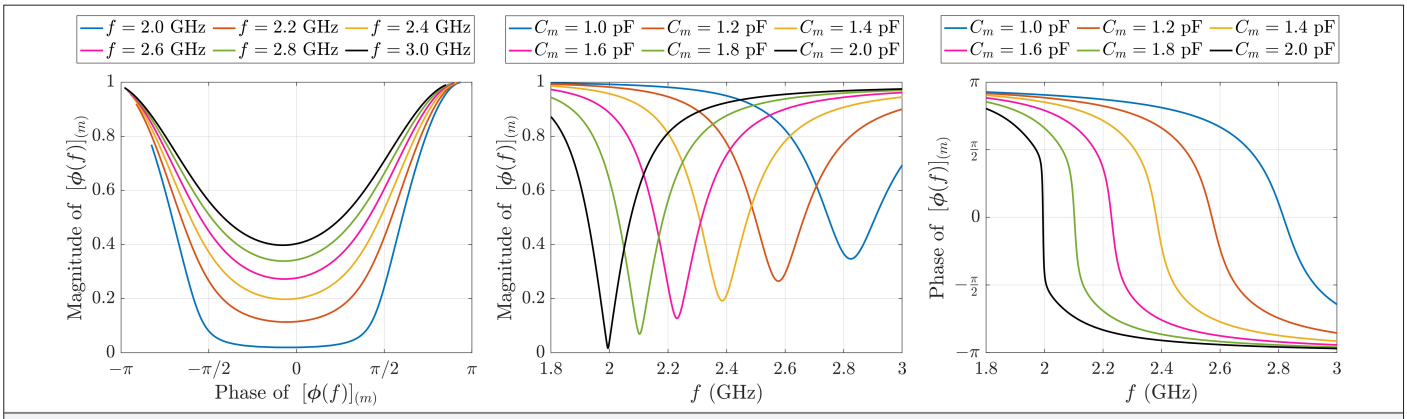

Fig. 2. Amplitude–phase–frequency coupling of an RIS element.

where L and J are the number of multipath components (MPCs) between the BS-RIS, and RIS-UE, respectively, $\bar{\alpha}_\ell$ and α_j are the random complex channel gains for the ℓth BS-RIS MPC and jth RIS-UE MPC, respectively, $\bar{\mathbf{u}}_k(\cdot)\in\mathbb{C}^{M\times 1}$ and $\mathbf{u}_k(\cdot)\in\mathbb{C}^{N\times 1}$ are the spatial wideband array response of the BS and the RIS, respectively, $\theta_\ell=\sin\tilde{\theta}_\ell$ is the sine of the physical AoA $\tilde{\theta}_\ell$ at the BS, $\varphi_\ell=\sin\tilde{\varphi}_\ell$ is the sine of the physical AoD $\tilde{\varphi}_\ell$ at the RIS, $\vartheta_j=\sin\tilde{\vartheta}_j$ is the sine of the physical AoA $\tilde{\vartheta}_j$ at the RIS, $f_k=f_c-\frac{W}{2}+(k-1)\frac{W}{N_c-1}$ for $k=1,2,\ldots,N_c$ is the discrete frequency value of the kth subcarrier, W is the signal bandwidth, f_c is the center frequency, and $\bar{\tau}_\ell\sim Unif\left[0,\bar{\tau}_{\max}\right]$ and $\tau_j\sim Unif\left[0,\tau_{\max}\right]$ are the propagation delays from the RIS to the BS and UE to the RIS, respectively. The spatial wideband array responses of the BS and RIS can be expressed as [24, 28]

$$\bar{\mathbf{u}}_k(\theta)=\left[1,e^{-i2\pi\frac{d_{BS}}{\lambda_c}\theta\frac{f_k}{f_c}},\ldots,e^{-i2\pi(M-1)\frac{d_{BS}}{\lambda_c}\theta\frac{f_k}{f_c}}\right]^T_{M\times 1}, \tag{6}$$

$$\mathbf{u}_k(\theta)=\left[1,e^{-i2\pi\frac{d_{RIS}}{\lambda_c}\theta\frac{f_k}{f_c}},\ldots,e^{-i2\pi(N-1)\frac{d_{RIS}}{\lambda_c}\theta\frac{f_k}{f_c}}\right]^T_{N\times 1}, \tag{7}$$

where d_{BS} and d_{RIS} are the antenna-spacing at the BS and the element spacing at the RIS, respectively, and λ_c is the wavelength for the center frequency. It is assumed that the first BS-RIS MPC ($\ell=1$) and the first RIS-UE MPC ($j=1$) are LOS, while all other MPCs are non-line-of-sight (NLOS). The LOS MPCs are modeled as the Rician components of their respective channels, with gains expressed as $\bar{\alpha}_1=\bar{\sigma}_1 e^{i\bar{\phi}}$ and $\alpha_1=\sigma_1 e^{i\phi}$, where $\bar{\sigma}_1^2$ and σ_1^2 represent the average power of the first BS-RIS and RIS-UE MPCs, respectively, and $\bar{\phi}$ and ϕ are the random phases. The NLOS MPCs are modeled as Rayleigh components, with gains expressed as $\bar{\alpha}_\ell\sim\mathcal{CN}\left(0,\bar{\sigma}_\ell^2\right)$ ($\ell>1$) and $\alpha_j\sim\mathcal{CN}\left(0,\sigma_j^2\right)$ ($j>1$), where $\bar{\sigma}_\ell^2$ and σ_j^2 represent the average power of the ℓth BS-RIS MPC and the jth RIS-UE MPC, respectively. The SNR is defined as $\mathrm{SNR}\triangleq M\left(\sum_{\ell=1}^{L}\bar{\sigma}_\ell^2\right)\left(\sum_{j=1}^{J}\sigma_j^2\right)/N_0$.

The received signal in (3) is rewritten using (4) and (5) as

$$\mathbf{y}_k=\sum_{\ell=1}^{L}\sum_{j=1}^{J}\alpha_{\ell,j}e^{-i2\pi f_k\tau_{\ell,j}}\left[\phi_k^T\mathbf{u}_k\left(\varrho_{\ell,j}\right)\right]\bar{\mathbf{u}}_k(\theta_\ell)x_k+\mathbf{n}_k, \tag{8}$$

where $\alpha_{\ell,j}\triangleq\bar{\alpha}_\ell\alpha_j$ is the cascaded channel gain, $\tau_{\ell,j}\triangleq\bar{\tau}_\ell+\tau_j$ is the cascaded delay, and $\varrho_{\ell,j}\triangleq\vartheta_j-\varphi_\ell$ is the cascaded angle. In this paper, the slowly-varying channel parameters, which are the average power of the cascaded gains $\sigma_{\ell,j}^2\triangleq\bar{\sigma}_\ell^2\sigma_j^2$, the cascaded angles $\varrho_{\ell,j}$, and the BS-side AoAs θ_ℓ are assumed to be known perfectly. These slowly-varying parameters can be estimated using the techniques described in refs. [27, 28].

IV. AMPLITUDE–PHASE–FREQUENCY COUPLING- AND BEAM-SQUINT-AWARE STATISTICAL RIS BEAMFORMING

In this section, beam-squint-aware (BSA) and APFC-aware (APFCA) statistical quantized RIS designs are proposed. Statistical optimization metrics, including output SNR, mean SMI, and a capacity upper bound based on C-CCM, are used. Accordingly, SNR-based, SMI-based, and C-CCM-based RIS designs are presented. The proposed quantized RIS designs are derived by adjusting the capacitance values of the RIS elements. For a q-bit quantized RIS design, the capacitance values are chosen from the set $\mathcal{C}_q$, where $|\mathcal{C}_q|=2^q$. The set $\mathcal{C}_q$ is constructed to ensure that the capacitance values within it yield uniformly quantized phase values for the center frequency, namely $\left\{0,\frac{2\pi}{2^q},\ldots,\left(2^q-1\right)\frac{2\pi}{2^q}\right\}$.

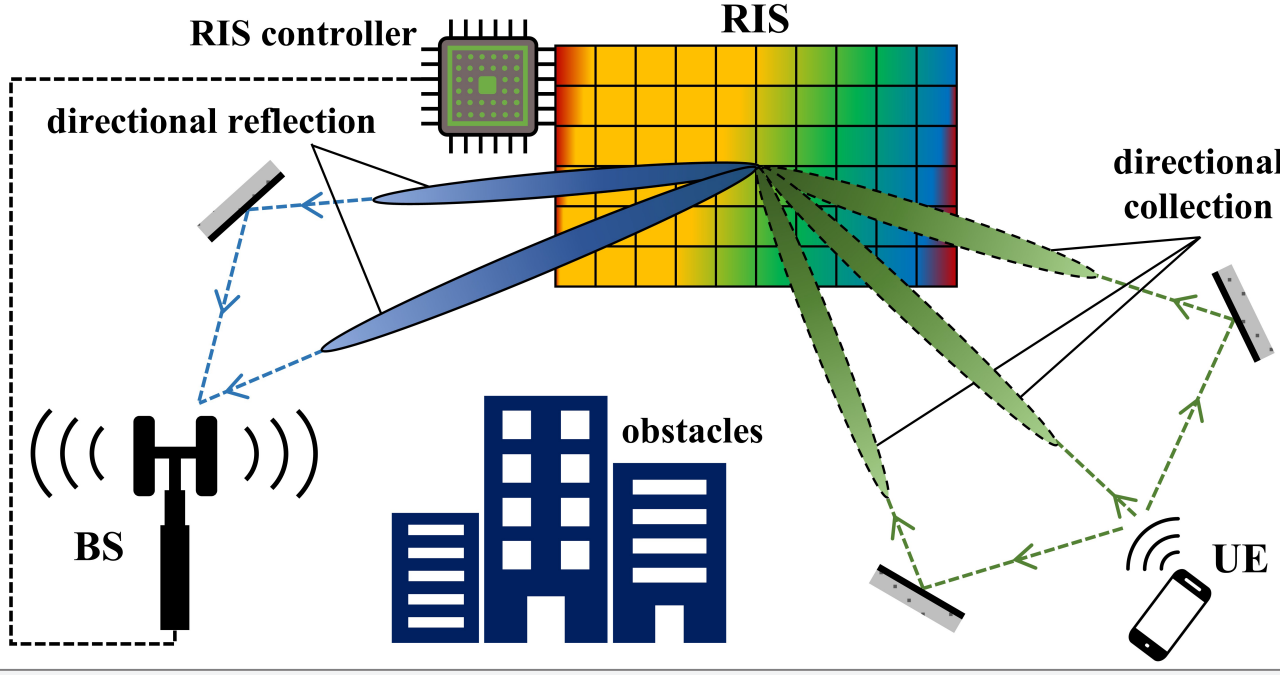

Fig. 3. System Scenario Description for RIS-aided MIMO.

A. Signal-to-Noise Ratio-Based Amplitude–Phase–Frequency Coupling-Aware Reconfigurable Intelligent Surface Design

Let $\mathbf{s}_k \triangleq \mathbf{g}_k x_k = \mathbf{H}_k \mathrm{diag}(\phi_k)\mathbf{h}_k x_k \in \mathbb{C}^{M\times 1}$ in (3) denote the user's signal in the frequency domain for the kth subcarrier, and $\bar{\mathbf{s}}_n$ represent the time domain signal at the nth time instance corresponding to the frequency domain signal $\mathbf{s}_k$, i.e., $\bar{\mathbf{s}}_n = \frac{1}{\sqrt{N_c}}\sum_{k=1}^{N_c}\mathbf{s}_k e^{j\frac{2\pi}{N_c}(k-1)n}$. The frequency domain and time domain covariance matrices are defined as $\mathbf{R}_{\mathbf{s}_k} \triangleq \mathbb{E}\left\{\mathbf{s}_k\mathbf{s}_k^H\right\} \in \mathbb{C}^{M\times M}$ and $\mathbf{R}_{\bar{\mathbf{s}}_n} \triangleq \mathbb{E}\left\{\bar{\mathbf{s}}_n\bar{\mathbf{s}}_n^H\right\} \in \mathbb{C}^{M\times M}$, respectively. The frequency domain covariance matrix can be calculated using (8) as

$$\mathbf{R}_{\mathbf{s}_k} = \sum_{\ell=1}^{L}\left[\sum_{j=1}^{J}\sigma_{\ell,j}^2\left|\phi_k^T\mathbf{u}_k\left(\varrho_{\ell,j}\right)\right|^2\right]\bar{\mathbf{u}}_k\left(\theta_\ell\right)\bar{\mathbf{u}}_k^H\left(\theta_\ell\right). \tag{9}$$

The relationship between the time domain and frequency domain covariance matrices for spatial wideband systems can be given according to Appendix A as $\mathbf{R}_{\bar{\mathbf{s}}_n} = \frac{1}{N_c}\sum_{k=1}^{N_c}\mathbf{R}_{\mathbf{s}_k}$. Then, the output SNR before the BS processing can be given using (9) as

$$\begin{aligned}\mathrm{SNR}_{\mathrm{out}} &\triangleq \frac{\mathbb{E}\left\{\|\,\bar{\mathbf{s}}_n{}^2\,\|\right\}}{N_0} = \frac{\mathrm{Tr}\left\{\mathbf{R}_{\bar{\mathbf{s}}_n}\right\}}{N_0} = \frac{1}{N_0}\mathrm{Tr}\left\{\frac{1}{N_c}\sum_{k=1}^{N_c}\mathbf{R}_{\mathbf{s}_k}\right\}\\ &= \frac{1}{N_0}\frac{M}{N_c}\sum_{k=1}^{N_c}\sum_{\ell=1}^{L}\sum_{j=1}^{J}\sigma_{\ell,j}^2\left|\phi_k^T\mathbf{u}_k\left(\varrho_{\ell,j}\right)\right|^2.\end{aligned} \tag{10}$$

The alternating optimization (AO)-based search algorithm from refs. [25, 29], referred to as the iterative phase refinement (IPR) algorithm, is adopted to maximize the output SNR. To reduce computational complexity, sub-band processing is implemented by utilizing only a fraction of the subcarriers, rather than all available subcarriers, because the frequency-dependent CCM does not change drastically across neighboring subcarriers [30]. Consequently, the output SNR in (10) is evaluated using the subcarrier indexes from the set $\mathcal{N}_c \triangleq \left\{1, \left\lfloor\frac{N_c}{N_c'-1}\right\rfloor, \left\lfloor\frac{2N_c}{N_c'-1}\right\rfloor, \ldots, N_c\right\}$, with $|\mathcal{N}_c| = N_c' \ll N_c$. Thus, the cost function to be maximized can be written as

$$\mathcal{J}_{\mathrm{cost}}^{(\mathrm{SNR})} \triangleq \frac{1}{N_0}\frac{M}{N_c'}\sum_{k\in\mathcal{N}_c}\sum_{\ell=1}^{L}\sum_{j=1}^{J}\sigma_{\ell,j}^2\left|\phi_k^T\mathbf{u}_k\left(\varrho_{\ell,j}\right)\right|^2. \tag{11}$$

This cost function can be maximized using Algorithm 1.

B. Statistical Mutual Information-Based Amplitude–Phase–Frequency Coupling-Aware Reconfigurable Intelligent Surface Design

The SMI between the user's signal $\mathbf{s}_k$ that passes through the channel and the received signal $\mathbf{y}_k$ in (8) can be expressed as [31]

$$I_k\left(\mathbf{s}_k, \mathbf{y}_k\right) = I_k\left(\mathbf{g}_k x_k, \mathbf{y}_k\right) = \log_2\left(\det\left|\mathbf{I}_M + \frac{1}{N_0}\mathbf{R}_{\mathbf{s}_k}\right|\right), \tag{12}$$

if $\mathbf{s}_k$ and $\mathbf{y}_k$ are assumed to be Gaussian. It can be calculated asymptotically when $M \to \infty$ according to Appendix B as

$$I_k\left(\mathbf{s}_k, \mathbf{y}_k\right) \approx \sum_{\ell=1}^{L}\log_2\left(1 + \frac{M}{N_0}\sum_{j=1}^{J}\sigma_{\ell,j}^2\left|\phi_k^T\mathbf{u}_k\left(\varrho_{\ell,j}\right)\right|^2\right). \tag{13}$$

Derived from the mutual information, the mean SMI metric is used, which is averaged over frequency, resulting in a single cost function. Then, utilizing sub-band implementation, the cost function to be maximized for the SMI-based RIS design is defined as $\mathcal{J}_{\mathrm{cost}}^{(\mathrm{SMI})} \triangleq \frac{1}{N_c'}\sum_{k\in\mathcal{N}_c} I_k\left(\mathbf{s}_k, \mathbf{y}_k\right)$, which can be expressed using (13) as

$$\mathcal{J}_{\mathrm{cost}}^{(\mathrm{SMI})} = \frac{1}{N_c'}\sum_{k\in\mathcal{N}_c}\sum_{\ell=1}^{L}\log_2\left(1 + \frac{M}{N_0}\sum_{j=1}^{J}\sigma_{\ell,j}^2\left|\phi_k^T\mathbf{u}_k\left(\varrho_{\ell,j}\right)\right|^2\right). \tag{14}$$

This cost function can be maximized using Algorithm 1.

C. Cascaded Channel Covariance Matrix-Based Amplitude–Phase–Frequency Coupling-Aware Reconfigurable Intelligent Surface Design

The received signal in (8) can be rewritten as

$$\mathbf{y}_k = \mathbf{G}_k\phi_k x_k + \mathbf{n}_k = \mathbf{g}_k x_k + \mathbf{n}_k, \tag{15}$$

where $\mathbf{G}_k \triangleq \mathbf{H}_k\mathrm{diag}(\mathbf{h}_k) \in \mathbb{C}^{M\times N}$ and $\mathbf{g}_k = \mathbf{G}_k\phi_k \in \mathbb{C}^{M\times 1}$. The achievable rate for a given channel realization $\mathbf{g}_k$ can be calculated using (15) as

$$\begin{aligned}C &\triangleq \frac{1}{N_c}\sum_{k=1}^{N_c} I_k\left(x_k, \mathbf{y}_k \,|\, \mathbf{g}_k\right)\\ &= \frac{1}{N_c}\sum_{k=1}^{N_c}\log_2\left(\det\left|\mathbf{I}_M + \frac{1}{N_0}\mathbf{g}_k\mathbf{g}_k^H\right|\right)\\ &= \frac{1}{N_c}\sum_{k=1}^{N_c}\log_2\left(1 + \frac{1}{N_0}\mathbf{g}_k^H\mathbf{g}_k\right)\\ &= \frac{1}{N_c}\sum_{k=1}^{N_c}\log_2\left(1 + \frac{1}{N_0}\phi_k^H\mathbf{G}_k^H\mathbf{G}_k\phi_k\right),\end{aligned} \tag{16}$$

if x_k is assumed to be Gaussian. Then, the ergodic capacity can be calculated and upper-bounded by Jensen's inequality as

$$\begin{aligned}\mathbb{E}\{C\} &= \mathbb{E}\left\{\frac{1}{N_c}\sum_{k=1}^{N_c}\log_2\left(1 + \frac{1}{N_0}\phi_k^H\mathbf{G}_k^H\mathbf{G}_k\phi_k\right)\right\}\\ &\le \frac{1}{N_c}\sum_{k=1}^{N_c}\log_2\left(1 + \frac{1}{N_0}\phi_k^H\mathbb{E}\left\{\mathbf{G}_k^H\mathbf{G}_k\right\}\phi_k\right)\\ &= \frac{1}{N_c}\sum_{k=1}^{N_c}\log_2\left(1 + \frac{M}{N_0}\phi_k^H\mathbf{R}_k\phi_k\right),\end{aligned} \tag{17}$$

where $\mathbf{R}_k \triangleq \frac{1}{M}\mathbb{E}\left\{\mathbf{G}_k^H\mathbf{G}_k\right\}$ is the C-CCM. The C-CCM can be calculated analytically using (4), (5), and (15) as

$$\mathbf{R}_k = \sum_{\ell=1}^{L}\sum_{j=1}^{J}\sigma_{\ell,j}^2\mathbf{u}_k^*\left(\varrho_{\ell,j}\right)\mathbf{u}_k^T\left(\varrho_{\ell,j}\right). \tag{18}$$

Notably, the ergodic capacity upper bound in (17) depends on slowly-varying channel parameters rather than on instantaneous channel realizations. Utilizing sub-band implementation, the cost function can be written using (17) and (18) as

$$\mathcal{J}_{\text{cost}}^{(\text{C-CCM})} \triangleq \frac{1}{N_c'} \sum_{k \in \mathcal{N}_c} \log_2\left(1+\frac{M}{N_0}\boldsymbol{\phi}_k^H \mathbf{R}_k \boldsymbol{\phi}_k\right) = \frac{1}{N_c'} \sum_{k \in \mathcal{N}_c} \log_2\left(1+\frac{M}{N_0}\sum_{\ell=1}^{L}\sum_{j=1}^{J}\sigma_{\ell,j}^2 \left|\boldsymbol{\phi}_k^T \mathbf{u}_k\left(\varrho_{\ell,j}\right)\right|^2\right). \tag{19}$$

This cost function can be maximized using Algorithm 1.

V. COMPLEXITY AND PERFORMANCE EVALUATIONS

A. Complexity of the Proposed Reconfigurable Intelligent Surface Beamforming

Several other RIS designs are included in the simulation results for comparison. Let $\boldsymbol{\phi}_{\text{DFT}} \in \mathbb{C}^{N\times 1}$ represent the unconstrained discrete Fourier transform (DFT)-based RIS design, which directs its beam towards the most dominant cascaded MPC (C-MPC) among the *LJ* C-MPCs by selecting the corresponding column of the DFT matrix [31]. This approach aligns with the RIS beamforming method proposed in ref. [32], where the authors adjust the RIS phases to match the strongest channel impulse response (CIR). Additionally, let $\boldsymbol{\phi}_{\text{Conv-EB}} \in \mathbb{C}^{N\times 1}$ denote the frequency-independent, beam-squint-unaware unconstrained design that maximizes the output SNR at the center frequency. This design corresponds to the most dominant eigenvector of the covariance matrix $\sum_{\ell=1}^{L}\sum_{j=1}^{J}\sigma_{\ell,j}^2 \mathbf{u}^*\left(\varrho_{\ell,j}\right)\mathbf{u}^T\left(\varrho_{\ell,j}\right)$ [31, 33], where $\mathbf{u}(x) \triangleq \left[1, e^{-i2\pi\frac{d_{\text{RIS}}}{\lambda_c}x}, \ldots, e^{-i2\pi(N-1)\frac{d_{\text{RIS}}}{\lambda_c}x}\right]^T$ is the conventional spatial narrowband RIS array response. This solution can be extended to account for beam-squint. Let $\boldsymbol{\phi}_{\text{BSA-EB}} \in \mathbb{C}^{N\times 1}$ represent the optimal frequency-independent unconstrained BSA design that maximizes the output SNR by considering BSE. This design corresponds to the most dominant eigenvector of the covariance matrix $\sum_{k=1}^{N_c}\sum_{\ell=1}^{L}\sum_{j=1}^{J}\sigma_{\ell,j}^2 \mathbf{u}_k^*\left(\varrho_{\ell,j}\right)\mathbf{u}_k^T\left(\varrho_{\ell,j}\right)$ [34], known as the eigenbeamformer (EB) solution. It's important to note that $\boldsymbol{\phi}_{\text{DFT}}$, $\boldsymbol{\phi}_{\text{Conv-EB}}$ and $\boldsymbol{\phi}_{\text{BSA-EB}}$ cannot be directly implemented due to the APFC constraint. To realize these designs in practice, it's necessary to determine the corresponding capacitance values for each RIS element. Once these capacitance values are determined, the resulting practical RIS designs adhere to the APFC model and no longer maintain frequency independence. These practical adaptations of the DFT-type beamformer and eigenbeamformers are designated as Conv.-DFT, Conv.-EB, and BSA-EB, respectively. The computational complexity orders and main features of the proposed RIS designs are given in Table I.

TABLE I. COMPUTATIONAL COMPLEXITY ORDERS AND MAIN FEATURES OF THE RIS DESIGNS

RIS Designs	Quant.	BSA	APFCA	Complexity
Conv. DFT [32]	✗	✗	✗	$O(N)$
Conv. EB [31]	✗	✗	✗	$O(LJN^2)$
BSA EB [34]	✗	✓	✗	$O(LJN_cN^2)$
SNR-based (proposed)	✓	✓	✓	$O(2^qLJN_{\text{iter}}N_cN^2)$
SMI-based (proposed)	✓	✓	✓	$O(2^qLJN_{\text{iter}}N_cN^2)$
C-CCM-based (proposed)	✓	✓	✓	$O(2^qLJN_{\text{iter}}N_cN^2)$

*APFCA, amplitude–phase–frequency-coupling-aware; BSA, beam-squint-aware; C-CCM, cascaded channel covariance matrix; Conv., conventional; DFT, discrete Fourier transform; EB, eigenbeamformer; Quant., quantized; RIS, reconfigurable intelligent surface; SMI, statistical mutualinformation; SNR, signal-to-noise ratio.

TABLE II. SIMULATION PARAMETERS

No. of BS antennas	$M=128$
No. of RIS elements	$N=128$
BS antenna spacing	$d_{\text{BS}}=\lambda_c/2$
RIS element spacing	$d_{\text{RIS}}=\lambda_c/2$
Center frequency	$f_c=2.4$ GHz
Signal bandwidth	$W=400$ MHz
No. of subcarriers	$N_c=1024$
Sub-band subcarriers	$N_c'=12$
No. of MPCs	$L=2, J=3$
BS-side AoAs	$\theta_\ell \sim Unif[-0.8, 0.8]\ \forall \ell$
Cascaded angles	$\varrho_{\ell,j} \sim Unif[-0.8, 0.8]\ \forall \ell, j$
MPC powers	$\bar{\sigma}_1^2/\bar{\sigma}_2^2 = \sigma_1^2/\sigma_2^2 = \sigma_2^2/\sigma_3^2 = 5$ dB
Propagation delays	$\bar{\tau}_{\max} = \tau_{\max} = 32/W$
RIS circuitry	$L_1=2.5$ nH, $L_2=0.7$ nH, $R=2.5\ \Omega$
Free space impedance	$Z_0=377\ \Omega$
IPR iterations	$N_{\text{iter}}=5$

*AoA, angle of arrival; BS, base station; IPR, iterative phase refinement; MPC, multipath component; No., number; RIS, reconfigurable intelligent surface.

B. *Simulation Results*

In this section, the simulation results are presented to demonstrate the performance of the proposed practical quantized RIS designs. The simulation parameters are presented in Table II. In the simulation results, the average SE (ASE) is presented, which is calculated by averaging the instantaneous achievable rates for given channel realizations over random UE locations.

The results of ASE vs. SNR and 10% outage capacity vs. SNR are presented in Figs. 4 and 5, respectively. These figures demonstrate that the proposed APFC-aware RIS designs (SNR-based, SMI-based, and C-CCM-based) outperform the APFC-unaware designs (Conv.-DFT, Conv.-EB, and BSA-EB). Notably, the C-CCM-based RIS design achieves 8 bits/s/Hz ASE at −5 dB SNR, while the BSA-EB requires 0 dB SNR to reach the same ASE. Similarly, the C-CCM-based RIS design reaches 6 bits/s/Hz 10% outage capacity at approximately −5 dB SNR, while the BSA-EB requires around 2 dB SNR to achieve the same 10% outage SE. This indicates that neglecting the APFC constraint can lead to a performance loss of around 5 dB for average SE and 7 dB for 10%

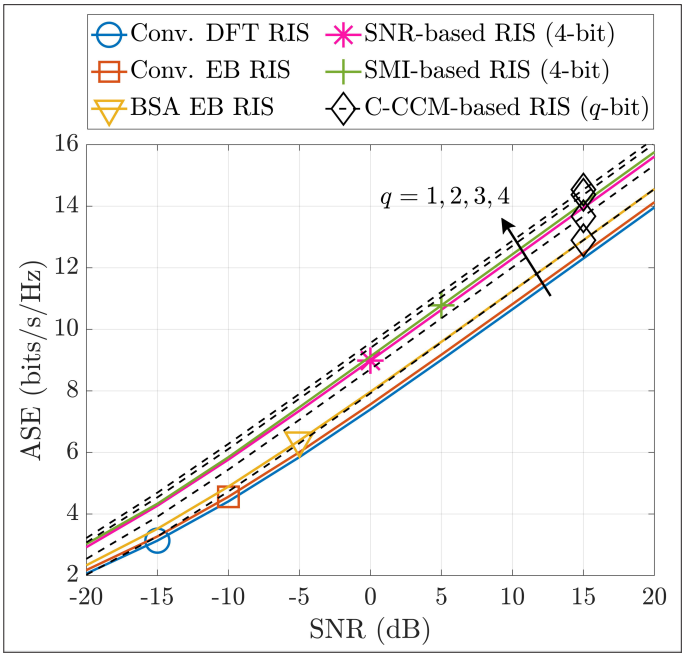

Fig. 4. Average Spectral Efficiency vs. SNR.

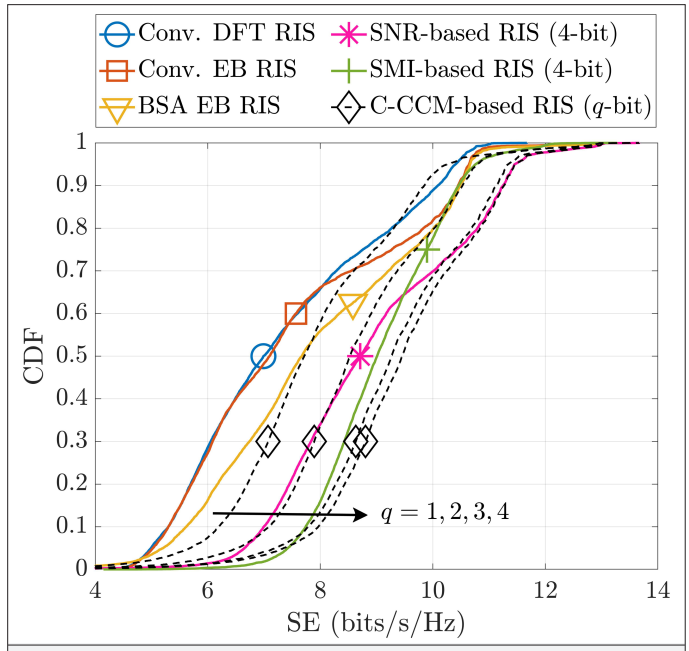

Fig. 6. CDF of Spectral Efficiency for SNR = 0 dB.

outage SE. Notably, these performance losses arise from neglecting the APFC in RIS beamforming design. It has been shown that disregarding such RIS hardware impairments also leads to significant degradation in channel estimation [28]. Consequently, the beamforming performance loss due to neglecting the APFC can compound with CSI acquisition errors, potentially causing more severe overall degradation, particularly in high-density and high-mobility environments. Additionally, the proposed C-CCM-based design surpasses the proposed SNR-based and SMI-based designs, which may indicate the potential significance of choosing an optimization metric that aligns closely with the ergodic capacity, as it serves as one of the ultimate benchmarks in wireless communication systems.

In Fig. 6, the cumulative distribution function (CDF) of the SE is presented. These CDF curves illustrate the outage probabilities for specific SE values, highlighting the robustness of the RIS designs to variations in UE locations. It is evident that disregarding the APFC results in significant degradation in outage performance, as shown by the fact that the 10% outage of Conv.-DFT, Conv.-EB, and BSA-EB falls below 6 bits/s/Hz, while the proposed C-CCM-based design achieves 8 bits/s/Hz at the 10% outage level.

Finally, in Fig. 7, the convergence of the IPR algorithm for the proposed C-CCM-based RIS design is illustrated. The IPR algorithm converges rapidly, typically within 3–4 iterations, making it feasible

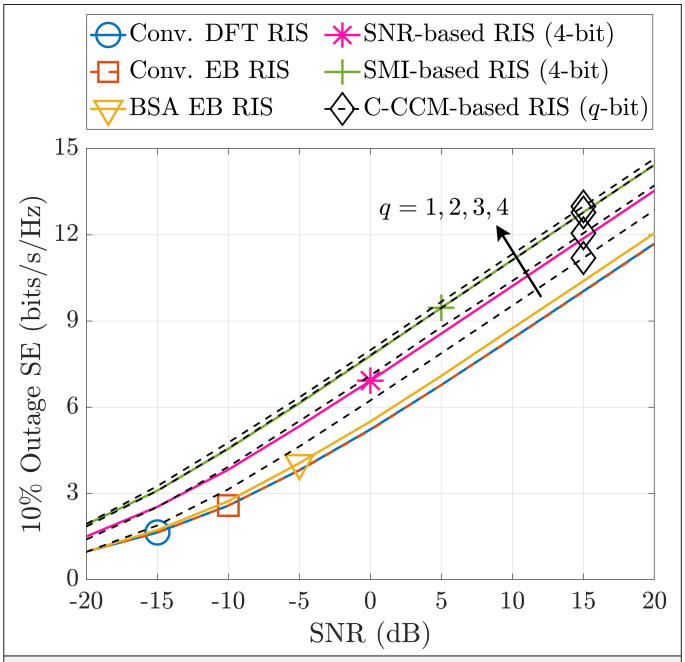

Fig. 5. 10% Outage Spectral Efficiency vs. SNR.

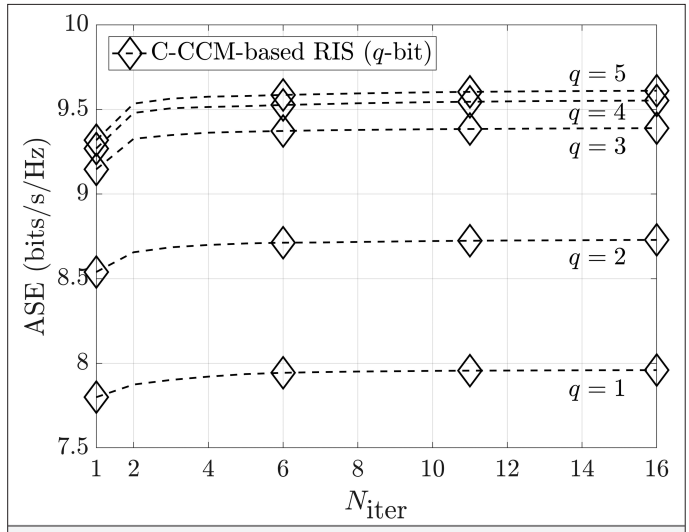

Fig. 7. ASE vs. number of IPR iterations for SNR = 0 dB.

for practical systems. Furthermore, the results indicate that increasing the quantization beyond 4 bits provides minimal performance gains, suggesting that the proposed C-CCM-based design with 4-bit quantization closely matches the performance of its unquantized counterpart. While higher quantization levels enhance ASE by enabling finer control over the RIS element phase shifts, they also lead to increased computational and hardware complexity. Notably, the infrequent updating of RIS beamforming due to the slowly varying nature of the C-CCM reduces the overall computational burden. Nonetheless, this trade-off can become particularly significant in scenarios where computational and hardware resources are limited. In such cases, lower quantization levels (e.g., 1-bit quantization) may be preferred, depending on the specific performance objectives. Notably, Figs. 4 and 5 demonstrate that the proposed 1-bit C-CCM-based design attains performance comparable to the unquantized BSA-EB, further highlighting its viability in resource-constrained scenarios.

VI. CONCLUSION

In this paper, the APFC constraint is investigated, and APFCA and BSA statistical quantized RIS beamforming designs are proposed. These designs, based on statistical metrics, do not rely on I-CSI, eliminating the need for frequent updates. Signal-to-Noise Ratio-based, SMI-based, and C-CCM-based RIS designs are introduced, with results demonstrating the superior performance of the C-CCM-based design compared to the SNR-based and SMI-based alternatives. To optimize these metrics, the IPR algorithm is employed, which converges rapidly within three to four iterations. Moreover, simulation results show that the proposed C-CCM-based RIS design with 4-bit quantization closely matches its unquantized counterpart, enhancing its feasibility for practical systems. Additionally, the proposed RIS designs are compared with conventional beamforming approaches, showing that conventional designs require up to 5 dB more power to achieve the same SE. As a future research direction, the proposed approaches can be extended to different RIS frameworks, such as RIS-aided integrated sensing and communication, adjustable-delay RIS, and stacked intelligent metasurface systems. Investigating the APFC constraint and the BSE within these contexts could provide valuable insights and make a meaningful contribution to the field.

Data Availability Statement: The data that support the findings of this study are available on request from the corresponding author.

Peer-review: Externally peer-reviewed.

Author Contributions: Concept – H.O., G.M.G.; Design – H.O., G.M..G.; Supervision – G.M.G.; Resources – H.O., G.M.G.; Materials – H.O., G.M.G.; Data Collection and/or Processing – H.O.; Analysis and/or Interpretation – H.O., G.M.G.; Literature Search – H.O., G.M.G.; Writing – H.O.; Critical Review – H.O., G.M.G.

Declaration of Interests: The authors have no conflict of interest to declare.

Funding: This study is supported by the folowing:

- The Scientific and Technological Research Council of Türkiye (TUBITAK) under the 2211-A Program.
- The Information and Communication Technologies Authority (ICTA) of Türkiye under the 5G and Beyond Joint Graduate Support Program.
- Vodafone Türkiye under the 5G and Beyond Joint Graduate Support Program.

REFERENCES

1. Y. Liu *et al.*, "Reconfigurable intelligent surfaces: Principles and opportunities," *IEEE Commun. Surv. Tutor.*, vol. 23, no. 3, pp. 1546–1577, 2021. [CrossRef]
2. J. An *et al.*, "Codebook-based solutions for reconfigurable intelligent surfaces and their open challenges," *IEEE Wirel. Commun.*, vol. 31, no. 2, pp. 134–141, 2024. [CrossRef]
3. C. Pan *et al.*, "Reconfigurable intelligent surfaces for 6g systems: Principles, applications, and research directions," *IEEE Commun. Mag.*, vol. 59, no. 6, pp. 14–20, 2021. [CrossRef]
4. A. Magbool, V. Kumar, and M. F. Flanagan, "Robust beamforming design for fairness-aware energy efficiency maximization in RIS-assisted mmWave communications," *IEEE Trans. Commun.*, pp. 1–1, 2025. [CrossRef]
5. F. Zhu *et al.*, "Robust beamforming for RIS-aided communications: Gradient-based manifold meta learning," *IEEE Trans. Wirel. Commun.*, vol. 23, no. 11, pp. 15945–15956, 2024. [CrossRef]
6. N. U. Saqib, S. Hou, S. H. Chae, and S.-W. Jeon, "Reconfigurable intelligent surface aided hybrid beamforming: Optimal placement and beamforming design," *IEEE Trans. Wirel. Commun.*, vol. 23, no. 9, pp. 12003–12019, 2024. [CrossRef]
7. J. An, C. Xu, D. W. K. Ng, C. Yuen, and L. Hanzo, "Adjustable delay RIS is capable of improving OFDM systems," *IEEE Trans. Veh. Technol.*, vol. 73, no. 7, pp. 9927–9942, 2024. [CrossRef]
8. B. O. Zhu, J. Zhao, and Y. Feng, "Active impedance metasurface with full 360◦ reflection phase tuning," *Sci. Rep.*, vol. 3, no. 1, p. 3059, 2013. [CrossRef]
9. W. Cai, H. Li, M. Li, and Q. Liu, "Practical modeling and beamforming for intelligent reflecting surface aided wideband systems," *IEEE Commun. Lett.*, vol. 24, no. 7, pp. 1568–1571, 2020. [CrossRef]
10. W. Cai, R. Liu, M. Li, Y. Liu, Q. Wu, and Q. Liu, "IRS-assisted multicell multiband systems: Practical reflection model and joint beamforming design," *IEEE Trans. Commun.*, vol. 70, no. 6, pp. 3897–3911, 2022. [CrossRef]
11. A. Khaleel, and E. Basar, "Phase shift-free passive beamforming for reconfigurable intelligent surfaces," *IEEE Trans. Commun.*, vol. 70, no. 10, pp. 6966–6976, 2022. [CrossRef]
12. Q. Wu, and R. Zhang, "Towards smart and reconfigurable environment: Intelligent reflecting surface aided wireless network," *IEEE Commun. Mag.*, vol. 58, no. 1, pp. 106–112, 2020. [CrossRef]
13. J. An, C. Xu, L. Gan, and L. Hanzo, "Low-complexity channel estimation and passive beamforming for RIS-assisted MIMO systems relying on discrete phase shifts," *IEEE Trans. Commun.*, vol. 70, no. 2, pp. 1245–1260, 2022. [CrossRef]
14. L. Li *et al.*, Cui,"Machine-learning reprogrammable metasurface imager," *Nat. Commun.*, vol. 10, no. 1, p. 1082, 2019.
15. W. Tang *et al.*, "Wireless communications with reconfigurable intelligent surface: Path loss modeling and experimental measurement," *IEEE Trans. Wirel. Commun.*, vol. 20, no. 1, pp. 421–439, 2021. [CrossRef]
16. X. Ma, D. Zhang, M. Xiao, C. Huang, and Z. Chen, "Cooperative beamforming for RIS-aided cell-free massive MIMO networks," *IEEE Trans. Wirel. Commun.*, vol. 22, no. 11, pp. 7243–7258, 2023. [CrossRef]
17. J. Yao, J. Xu, W. Xu, D. W. K. Ng, C. Yuen, and X. You, "Robust beamforming design for RIS-aided cell-free systems with CSI uncertainties and capacity-limited backhaul," *IEEE Trans. Commun.*, vol. 71, no. 8, pp. 4636–4649, 2023. [CrossRef]
18. K. Zhong *et al.*, "RIS-aided beamforming design for MIMO systems via unified manifold optimization," *IEEE Trans. Veh. Technol.*, vol. 74, no. 1, pp. 1–11, 2024.
19. Y. Chen, D. Chen, T. Jiang, and L. Hanzo, "Channel-covariance and angle-of-departure aided hybrid precoding for wideband multiuser millimeter wave MIMO systems," *IEEE Trans. Commun.*, vol. 67, no. 12, pp. 8315–8328, 2019. [CrossRef]
20. W. Shen, L. Dai, B. Shim, Z. Wang, and R. W. Heath, "Channel feedback based on AoD-adaptive subspace codebook in FDD massive MIMO systems," *IEEE Trans. Commun.*, vol. 66, no. 11, pp. 5235–5248, 2018. [CrossRef]
21. Y. Chen, D. Chen, and T. Jiang, "Non-uniform quantization codebook-based hybrid precoding to reduce feedback overhead in millimeter wave MIMO systems," *IEEE Trans. Commun.*, vol. 67, no. 4, pp. 2779–2791, 2019. [CrossRef]
22. V. Va, J. Choi, and R. W. Heath, "The impact of beamwidth on temporal channel variation in vehicular channels and its implications," *IEEE Trans. Veh. Technol.*, vol. 66, no. 6, pp. 5014–5029, 2017. [CrossRef]

23. B. Wang *et al.*, "Spatial-wideband effect in massive MIMO with application in mmWave systems," *IEEE Commun. Mag.*, vol. 56, no. 12, pp. 134–141, 2018. [CrossRef]
24. B. Wang, F. Gao, S. Jin, H. Lin, and G. Y. Li, "Spatial- and frequency-wideband effects in millimeter-wave massive MIMO systems," *IEEE Trans. Signal Process.*, vol. 66, no. 13, pp. 3393–3406, 2018. [CrossRef]
25. H. Ozen, and G. M. Guvensen, "A robust quantized beam-squint and interference aware statistical beamforming for RIS-aided massive MIMO," in ICC 2023 - IEEE Int. Conf. Commun. IEEE, 2023, pp. 1307–1312. [CrossRef].
26. E. K. Hidir, E. Basar, and H. A. Cirpan, "On practical RIS-aided OFDM with index modulation," *IEEE Access*, vol. 11, pp. 13113–13120, 2023. [CrossRef]
27. G. Zhou, C. Pan, H. Ren, P. Popovski, and A. L. Swindlehurst, "Channel estimation for RIS-aided multiuser millimeter-Wave systems," *IEEE Trans. Signal Process.*, vol. 70, pp. 1478–1492, 2022. [CrossRef]
28. H. Ozen, O. Yilmaz, and G. M. Guvensen, "Beam-squint-aware channel estimation for dual-wideband UPA-type RIS-aided massive MIMO," *IEEE Commun. Lett.*, vol. 28, no. 10, pp. 2367–2371, 2024. [CrossRef]
29. S. Abeywickrama, R. Zhang, Q. Wu, and C. Yuen, "Intelligent reflecting surface: Practical phase shift model and beamforming optimization," *IEEE Trans. Commun.*, vol. 68, no. 9, pp. 5849–5863, 2020. [CrossRef]
30. H. Ozen, and G. M. Guvensen, "Interference and beam squint aware TTD-aided beamforming for dual wideband massive MIMO," *IEEE Wirel. Commun. Lett.*, vol. 13, no. 1, pp. 64–68, 2024. [CrossRef]
31. M. Bayraktar, and G. M. Guvensen, "An efficient interference-aware constrained massive MIMO beamforming for mm-Wave JSDM," *IEEE Access*, vol. 9, pp. 87877–87897, 2021. [CrossRef]
32. B. Zheng, and R. Zhang, "Intelligent reflecting surface-enhanced OFDM: Channel estimation and reflection optimization," *IEEE Wirel. Commun. Lett.*, vol. 9, no. 4, pp. 518–522, 2020. [CrossRef]
33. H. Ozen, "*An Interference and Beam Squint Aware Hybrid Massive MIMO for Spatial Wideband BDMA Channels*", Master's thesis. Middle East Technical Univ., 2022.
34. G. Femenias, and F. Riera-Palou, "Wideband cell-free mmWave massive MIMO-OFDM: Beam squint-aware channel covariance-based hybrid beamforming," *IEEE Trans. Wirel. Commun.*, vol. 21, no. 7, pp. 4695–4710, 2022. [CrossRef]

Hakan Özen received his B.S. and M.S. degrees in Electrical and Electronics Engineering from Middle East Technical University (METU), Ankara, Türkiye, in 2019 and 2022, respectively. He is currently pursuing a Ph.D. degree in the Department of Electrical and Electronics Engineering at METU. His research interests include signal processing for wireless communications, with a particular focus on mmWave massive MIMO and RIS-aided systems.

Dr. Gökhan M. Güvensen received his BS, MS, and Ph.D. degrees in electrical and electronics engineering from the Middle East Technical University (METU), Ankara, Türkiye in 2006, 2009 and 2014, respectively. He worked as a postdoctoral fellow in the Center for Pervasive Communications and Computing (CPCC) in the University of California, Irvine (UCI), USA between 2015 and 2016. In 2017, he joined the Electrical and Electronics Engineering Department at METU, where he is now an Assistant Professor. He was the recipient of Leopold B. Felsen Award in 2018, which is given by the Leopold B. Felsen Foundation to Turkish researchers for their publications generated from their research. His research interests include the design of digital communication systems and statistical signal processing with a particular focus on modulation theory, next-generation mobile communication techniques, iterative detection and equalization, beamforming, radar signal processing, joint sensing and communication and MIMO Radar systems.

ALGORITHM 1. BSA–APFCA *Q*-BIT STATISTICAL RIS VIA IPR

Input: Slowly-varying channel parameters: $\sigma_{\ell,j}^2$, $\varrho_{\ell,j}$ $\forall \ell, j$

1: Set $\phi_k = \mathbf{0}_{N\times 1} \forall k \in \mathcal{N}_c$ # Initialization

2: **for** iter = 1 **to** N_{iter}

3: **for** $m = 1$ **to** N

4: Search for optimal $C^* \in \mathcal{C}_q$ so that

$$\left[\phi_k\right]_{(m)} = \frac{Z\left(C^*, f_k\right) - Z_0}{Z\left(C^*, f_k\right) + Z_0} \text{ maximizes } \mathcal{J}_{\text{cost}}^{(\text{C–CCM})} \text{ in}$$

(19) while $C_{m'}$'s are kept fixed for $m' \neq m$

5: Update $C_m = C^*$

6: Update $\left[\phi_k\right]_{(m)} = \dfrac{Z\left(C_m, f_k\right) - Z_0}{Z\left(C_m, f_k\right) + Z_0} \forall k \in \mathcal{N}_c$

7: **end**

8: **end**

Output: q-bit $C_m \forall m$, $\left[\phi_k\right]_{(m)} = \dfrac{Z\left(C_m, f_k\right) - Z_0}{Z\left(C_m, f_k\right) + Z_0} \forall m, k$

*BSA, beam-squint-aware; APFCA, amplitude–phase–frequency coupling aware; RIS, reconfigurable intelligent surface; IPR, iterative phase refinement.

APPENDIX A. TIME DOMAIN COVARIANCE MATRIX

$$\begin{aligned}
\mathbf{R}_{\bar{\mathbf{s}}_n} &\triangleq \mathbb{E}\left\{\bar{\mathbf{s}}_n \bar{\mathbf{s}}_n^H\right\} \\
&= \frac{1}{N_c}\mathbb{E}\left\{\left[\sum_{k=1}^{N_c} \mathbf{s}_k e^{i\frac{2\pi}{N_c}(k-1)n}\right]\left[\sum_{k=1}^{N_c} \mathbf{s}_k e^{i\frac{2\pi}{N_c}(k-1)n}\right]^H\right\} \\
&= \frac{1}{N_c}\mathbb{E}\left\{\left[\sum_{k=1}^{N_c} \mathbf{g}_k x_k e^{i\frac{2\pi}{N_c}(k-1)n}\right]\left[\sum_{k=1}^{N_c} \mathbf{g}_k x_k e^{i\frac{2\pi}{N_c}(k-1)n}\right]^H\right\} \\
&= \frac{1}{N_c}\mathbb{E}\left\{\sum_{k=1}^{N_c}\sum_{k'=1}^{N_c} \mathbf{g}_k \mathbf{g}_{k'}^H x_k x_{k'}^* e^{i\frac{2\pi}{N_c}(k-k')n}\right\} \qquad (20) \\
&= \frac{1}{N_c}\sum_{k=1}^{N_c}\sum_{k'=1}^{N_c}\mathbb{E}\left\{\mathbf{g}_k \mathbf{g}_{k'}^H\right\}\mathbb{E}\left\{x_k x_{k'}^*\right\} e^{i\frac{2\pi}{N_c}(k-k')n} \\
&= \frac{1}{N_c}\sum_{k=1}^{N_c}\sum_{k'=1}^{N_c}\mathbb{E}\left\{\mathbf{g}_k \mathbf{g}_{k'}^H\right\}\delta_{kk'} e^{i\frac{2\pi}{N_c}(k-k')n} \\
&= \frac{1}{N_c}\sum_{k=1}^{N_c}\mathbb{E}\left\{\mathbf{g}_k \mathbf{g}_k^H\right\} = \frac{1}{N_c}\sum_{k=1}^{N_c}\mathbf{R}_{\mathbf{s}_k}
\end{aligned}$$

APPENDIX B. MUTUAL INFORMATION CALCULATION

The expression of $\mathbf{R}_{\mathbf{s}_k}$ is given in (9). Note that $\bar{\mathbf{u}}_k^H\left(\theta_\ell\right)\bar{\mathbf{u}}_k\left(\theta_{\ell'}\right) = M\delta_{\ell\ell'}$ when $M \to \infty$ [27]. In other words, different MPCs are asymptotically orthogonal when $M \to \infty$. Thus, $\left\{\bar{\mathbf{u}}_k\left(\theta_\ell\right)\right\}_{\ell=1}^{L}$ become the orthogonal eigenvectors of $\mathbf{R}_{\mathbf{s}_k}$ when $M \to \infty$. Then, the expression of $\mathbf{R}_{\mathbf{s}_k}$ in (9) is indeed the spectral decomposition of $\mathbf{R}_{\mathbf{s}_k}$ when $M \to \infty$. Consequently, the non-zero eigenvalues of $\mathbf{R}_{\mathbf{s}_k}$ are found as $M\left\{\sum_{j=1}^{J}\sigma_{\ell,j}^2\left|\phi_k^T\mathbf{u}_k\left(\varrho_{\ell,j}\right)\right|^2\right\}_{\ell=1}^{L}$. Let $\lambda_{\ell,k}$ denote the ℓ^{th} eigenvalue of $\mathbf{R}_{\mathbf{s}_k}$, i.e., $\lambda_{\ell,k} = M\sum_{j=1}^{J}\sigma_{\ell,j}^2\left|\phi_k^T\mathbf{u}_k\left(\varrho_{\ell,j}\right)\right|^2$ for $1 \le \ell \le L$,and $\lambda_{\ell,k} = 0$ for $L < \ell \le M$. Let us re-express $\mathbf{R}_{\mathbf{s}_k}$ using eigen decomposition as $\mathbf{R}_{\mathbf{s}_k} = \mathbf{E}_k\Lambda_k\mathbf{E}_k^H$ such that $\mathbf{E}_k^H\mathbf{E}_k = \mathbf{I}_M$, and $\Lambda_k = \text{diag}\left(\lambda_{1,k},\ldots,\lambda_{L,k},0,0,\ldots,0\right) \in \mathbb{C}^{M\times M}$. Then the mutual information in (13) can be calculated as

$$\begin{aligned}
I_k\left(\mathbf{s}_k, \mathbf{y}_k\right) &= \log_2\left(\det\left|\mathbf{I}_M + \frac{1}{N_0}\mathbf{R}_{\mathbf{s}_k}\right|\right) \\
&= \log_2\left(\det\left|\mathbf{I}_M + \frac{1}{N_0}\mathbf{E}_k\Lambda_k\mathbf{E}_k^H\right|\right) \\
&= \log_2\left(\det\left|\mathbf{E}_k\left(\mathbf{I}_M + \frac{1}{N_0}\Lambda_k\right)\mathbf{E}_k^H\right|\right) \\
&= \log_2\left(\det\left|\left(\mathbf{I}_M + \frac{1}{N_0}\Lambda_k\right)\mathbf{E}_k^H\mathbf{E}_k\right|\right) \qquad (21) \\
&= \log_2\left(\det\left|\left(\mathbf{I}_M + \frac{1}{N_0}\Lambda_k\right)\right|\right) \\
&= \log_2\left(\prod_{\ell=1}^{L}\left(1 + \frac{1}{N_0}\lambda_{\ell,k}\right)\right) \\
&= \sum_{\ell=1}^{L}\log_2\left(1 + \frac{1}{N_0}\lambda_{\ell,k}\right),
\end{aligned}$$

which completes the proof.